Thermally Driven Interfacial Dynamics of Metal/Oxide Bilayer Nanoribbons

Matt Law, Xiao Feng Zhang, Rong Yu, Tevye Kuykendall, and Peidong Yang*

Solid–solid interfacial processes greatly affect the performance of electronic and composite materials, but probing the dynamics of buried interfaces is challenging and often involves lengthy or invasive sample preparation. We show that bilayer nanoribbons—made here of tin dioxide and copper—are convenient structures for observing as-made interfaces as they respond to changing temperature in a transmission electron microscope (TEM). At low temperatures ($<200\,°C$), differential thermal expansion causes the bilayers to bend when heated or cooled, with the motion determined by the extent of $Cu–SnO_2$ epitaxy. At higher temperatures, we are able to watch—in real time and with nanometer resolution—a progression of grain growth, interdiffusion, island formation, solid-state chemical reactions, and melting. This novel TEM geometry is readily applicable to other nanoribbon/coating combinations and is well suited to observing interfacial phenomena driven thermally or by the application of mechanical, electrical, or magnetic forces.

1. Introduction

In situ electron microscopy provides a means to directly visualize interfacial processes in real time and with high spatial resolution. Few other experimental methods are available for probing the dynamic structure of buried interfaces. Of these, synchrotron-based, all-photon X-ray spectroscopies[1,2] provide chemical information from the near-surface bulk of a sample, but lack spatial resolution. Traditional surface-sensitive techniques, including photoelectron spectroscopy and various scanning tunneling microscopies,[3,4] are largely limited to systems with ultrathin, smooth and/or conductive overlayers. Although TEM does not face these constraints, the preparation of electron-transparent samples from thin films requires a laborious sequence of cross-sectioning, thinning, and polishing steps that can undesirably alter the interface under study. An attractive strategy for eliminating such sample preparation is to deposit a layer of material onto a miniature substrate that is already electron-transparent and mounted for TEM imaging. As we demonstrate here, chemically synthesized nanoribbons[5] are ideal substrates for this purpose: They are of the appropriate thickness, available in a variety of materials with flat and well-defined surfaces (including single-crystals of silicon, oxides, carbides, nitrides, phosphides, and chalcogenides), and can form abrupt bilayer interfaces with solids that are deposited by vacuum methods such as thermal evaporation or pulsed-laser deposition. The bilayer nanoribbon is thus a promising experimental platform for studying as-made interfaces between inorganic crystals and inorganic, organic, or metal films. Previous in situ TEM studies have focused on such phenomena as the nucleation of films from atomic fluxes,[6] annealing-induced interfacial reactions,[7] and gas-induced shape changes of nanocrystals grown on oxide sup-

[*] M. Law,+ T. Kuykendall, Prof. P. Yang
     Department of Chemistry
     University of California, Berkeley
     Berkeley, California 94720 (USA)
     Fax: (+1) 510-642-7301
     E-mail: p_yang@berkeley.edu
     Dr. X. F. Zhang,+ Dr. R. Yu
     Materials Sciences Division
     Lawrence Berkeley National Laboratory
     Berkeley, California 94720 (USA)
[+] These authors contributed equally to this work.
     Supporting information for this article is available on the WWW under http://www.small-journal.com or from the author.

ports.[8] Of the handful of bilayer nanowires[9,10] and nano-ribbons[11] reported so far, none has yet been exploited in this type of fundamental investigation.

2. Results and Discussion

We use single-crystalline SnO_2 nanoribbons coated with copper as a model system. Metal films on oxide surfaces are technologically important in many applications, including oxide-supported catalysis, microelectronics, metal/ceramic composites, and gas sensing. Metal/oxide interfaces are also classic systems in the study of adhesion and corrosion. The crystallography of our SnO_2 nanoribbons is described in detail elsewhere.[11] The ribbons are rutile single crystals (tetragonal, with $a = 4.738$ Å and $c = 3.187$ Å) with quasi-rectangular cross sections and nearly atomically smooth facets. The ribbon samples typically have broad size distri-butions, with widths and thicknesses ranging from 10 nm to 1 μm, width/thickness ratios as high as ten, and lengths up to several millimeters. The ribbons are bounded by the $SnO_2(10\bar{1})$ and (010) surfaces and grow nearly along the [101] crystal direction.

Nanoribbons were used as substrates for the vapor depo-sition of thin Cu films to produce metal/oxide bilayers (see the Experimental Section and Figure S1 in the Supporting Information). TEM observations of bilayers prepared at room temperature reveal the existence of distinct structural types for growth on $SnO_2(10\bar{1})$ versus (010). Growth on the $(10\bar{1})$ surface produces dense and continuous films of Cu grains with no preferred orientation relative to the sub-strate. In contrast, Cu on $SnO_2(010)$ always forms flat and epitaxial Cu(111) films (Figure 1). We attribute this epitaxy to the small domain mismatch[12] ($\approx 0.1\%$) in the in-plane $Cu[10\bar{1}] || SnO_2[001]$ direction (Figure 2). On the other hand, epitaxy is frustrated on $(10\bar{1})$ by poor overlap be-tween the close-packed copper layer and the oxygen sublat-tice of SnO_2 on this surface. High-resolution imaging, select-ed-area electron diffraction (SAED), and energy-dispersive spectroscopy (EDS) show that the epi-bilayers have atomi-cally abrupt $Cu-SnO_2$ interfaces without detectable inter-mediate phases such as Cu_2O or Cu–Sn alloys. An abrupt in-terface is consistent with the low oxygen affinity of copper and weak $Cu-SnO_2$ bonding (see Ref. [13] and below). Both the untextured films and epi-films consist of equiaxed Cu grains of a size commensurate with the film thickness. We focus here on films 8–55 nm thick deposited on nanoribbons 25–200 nm thick.

The response of both untextured and epi-bilayers to in situ TEM heating can be loosely divided into three stages: bending, island formation, and etching. In the first stage, relevant to temperatures up to 200°C, the dissimilar thermal expansion coefficients of Cu (16.5×10^{-6} K^{-1}) and SnO_2 (3.8×10^{-6} K^{-1})[14] cause the bilayers to bend upon heating or cooling, analogous to the action of the sensing el-ement in a standard thermostat. The bilayers can be mod-eled as ultrasmall cantilevers with one end pinned to the TEM grid and the other end free. Classical beam theory
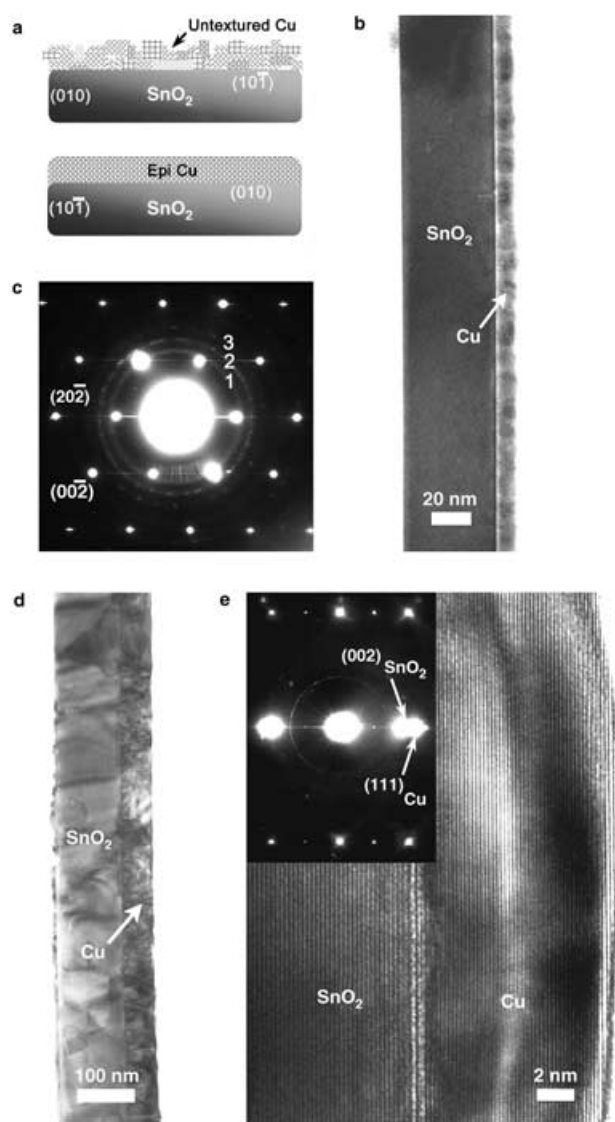

Figure 1. TEM characterization of $Cu-SnO_2$ bilayer nanoribbons: a) Cartoon cross sections (perpendicular to the long axis of the nano-ribbon) show that the thermal deposition of copper onto SnO_2 nano-ribbons yields untextured or epitaxial bilayers when the $(10\bar{1})$ or (010) surfaces are coated, respectively; b) a TEM image, and c) a dif-fraction pattern ($SnO_2[010]$ zone axis) of an 11-nm-thick untextured Cu layer on a 49-nm-thick ribbon demonstrate the absence of epitax-ial growth on $SnO_2(10\bar{1})$. Polycrystalline rings 1–3 are indexed to $Cu_2O(111)$, Cu(111), and Cu(200), respectively. The Cu_2O impurity was detected only in untextured bilayers that were fabricated in poor vacuum ($> 10^{-6}$ Torr); d) epitaxial copper layers grown on $SnO_2(010)$ have the orientation relationship $Cu(111)[10\bar{1}] || SnO_2(010)[001]$ and often feature complex strain contrast, as shown in this low-magnifi-cation image of a bilayer with a 55-nm-thick coating; e) a lattice-resolved image of a thinner epi-bilayer shows the abruptness of the $Cu-SnO_2$ interface. Imaging, EDS, and diffraction data (inset, $Cu[11\bar{2}] || SnO_2[103]$ zone axis) gave no evidence of additional phases.

states that a global temperature change, ΔT, should result in a displacement of the bilayer tip, Δd, given by[15]

$$\Delta d = 3\ell^2(\alpha_{Metal} - \alpha_{Oxide})\frac{t_{Metal} + t_{Oxide}}{t_{Oxide}^2 K}\Delta T \qquad (1)$$
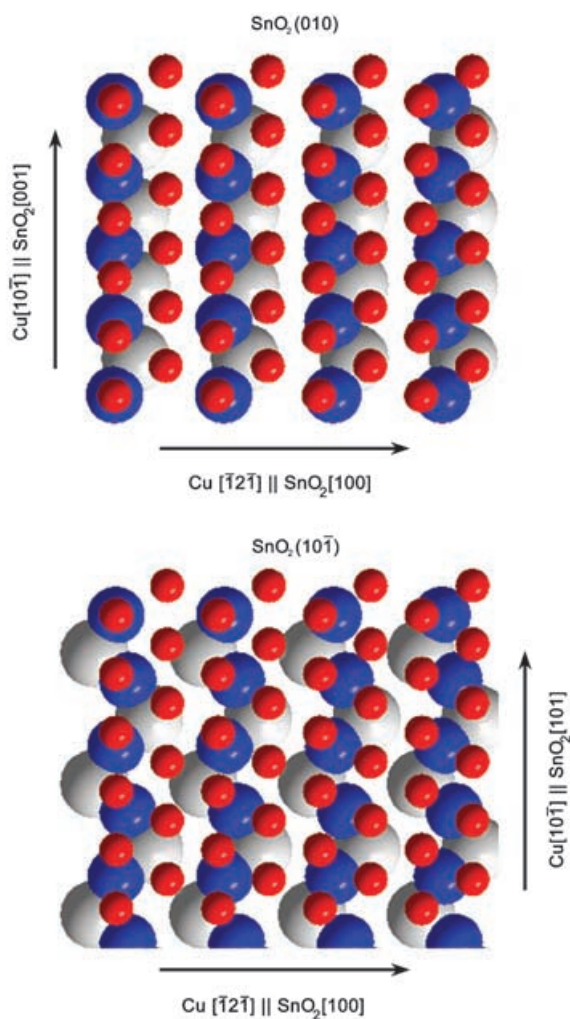
Figure 2. Atomic arrangements of Cu(111) on SnO$_2$(010) and (10$\bar{1}$). In the case of Cu(111)||SnO$_2$(010) epitaxy (top), the in-plane lattice mismatch is 6.7% and 19.9% in the SnO$_2$[100] and [001] directions, respectively. However, since every sixth copper atom overlaps to within 0.1% of every fifth oxygen atom in the [001] direction, domain-matching epitaxy is possible on this surface. No such favorable overlaps exist for the hypothetical Cu(111)||SnO$_2$(10$\bar{1}$) situation (bottom) and so the film is untextured. Here, the red, blue, and gray spheres represent copper, oxygen, and tin atoms, respectively.

where ℓ is the beam length, α is the expansion coefficient, t is the thickness, and K is a constant that includes the anisotropic Young's modulus of both materials. Figure 3 shows the typical bending response of an epitaxial and an untextured bilayer when subjected to repeated temperature cycles. We found that epi-bilayers bent elastically and reversibly, but with a 30–40% smaller tip displacement than expected from Equation (1). Since this expression neglects the three-dimensional elastic anisotropy of the crystalline Cu and SnO$_2$ layers, we performed finite element simulations of thermally induced bending with the FEMLAB 3.1 software package, using fully anisotropic bulk materials parameters[16,17] and the proper epitaxial orientation for the Cu and SnO$_2$ subdomains (See Supporting Information, Figure S2). Results from these models were in slightly poorer agreement with experiment, with displacements that were up to
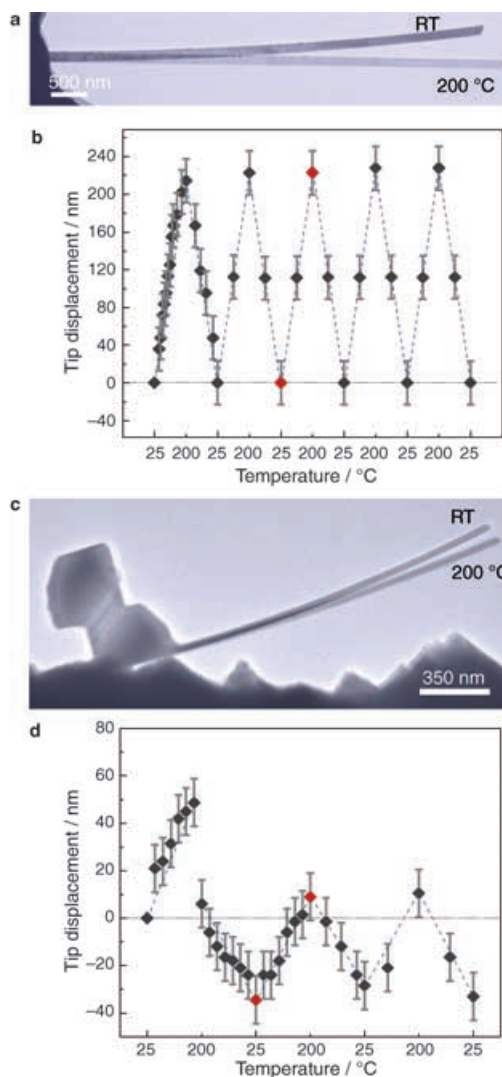

Figure 3. Bimetallic bending of epitaxial and untextured bilayers: a) Superimposed TEM images of an epi-bilayer (28 nm Cu on top, 90 nm SnO$_2$ on bottom, 6.1 µm long) at room temperature and 200 °C, showing a tip displacement of 225 ± 15 nm; b) the corresponding plot of tip displacement versus temperature illustrates that bending is linear with temperature and reversible through multiple heat–cool cycles. Deviation during the first cycle is caused by a release of residual stresses accumulated during the copper deposition. Points highlighted in red indicate the data extracted from the two images in (a); c) image, and d) temperature-displacement plot for an untextured bilayer (8.3 nm Cu on top, 24 nm SnO$_2$ on bottom, 1.77 µm long). Each non-epitaxial bilayer studied exhibited a plastic response during either the first or every temperature cycle. As shown in (d), grain movement within the stressed copper layer caused the bilayer to slip during the first ramp at ≈175 °C and then stabilize at a new curvature and tip displacement, far from the expected value based on its geometry.

42% larger than our TEM measurements. This discrepancy is unresolved, but could be explained if the thermal expansion constants or elastic moduli of Cu or SnO$_2$ take on non-bulk values in the thin bilayer geometry.[18]

In contrast to the reversible bending of the epi-bilayers, the untextured bilayers always displayed a degree of plastic deformation superimposed on an elastic displacement; some

samples slipped during the first heating ramp and then stabilized at a new tip amplitude (Figure 3 d), while others showed a progressive damping of motion without an initial catastrophic slip. We attribute the plastic deformation of the untextured cantilevers to grain rotation and sliding that commences above 125 °C. Grain motion is expected to be comparatively facile in the untextured films because their abundance of high-angle grain boundaries results in weaker intergrain cohesion and poorer grain–substrate adhesion. We note that dislocation-mediated plasticity is unlikely to be as important as grain sliding for the nanocrystalline copper investigated here.[19]

Prior to heating, as-made bilayers always showed a slight curvature toward the copper film. Calculations indicate that during deposition, the energy flux onto a ribbon from the combination of Cu condensation and radiative heating is sufficient to raise the ribbon temperature by up to 40 °C. Upon cooling, differential contraction creates interfacial stress that is partly accommodated by the elastic deformation of the entire bilayer. Alternative strain responses, such as the accumulation of misfit dislocations at the interface or partial delamination of the Cu film, were not observed, perhaps because the low rigidity of the thin ribbon substrate permits its facile deformation. During heating, the Cu film moves from an initial state of slight tensile stress to an increasing degree of compressive stress; for the epitaxial structures, this switchover is reversible with cooling.

These bilayers are among the smallest thermally actuated cantilevers reported to date and could be applied as thermometric sensors in nanoelectromechanical systems (NEMS). Because they are roughly an order of magnitude thinner than the commercially available micromachined cantilevers now used as prototype microcalorimeters[20] and molecular sensors,[21, 22] nanoribbon-based cantilevers have a temperature sensitivity that is 25–100 times higher (e.g., 4×10^{-5} K Å^{-1} for a Cu–SnO$_2$ bilayer 50 nm thick and 100 μm long), in addition to better stress sensitivity and faster response times. Ultrathin nanoribbons[23] may allow the fabrication of cantilevers that perform close to theoretical limits,[24] but only if challenges related to the mechanical resilience of thin heterointerfaces[25] and integrated motion detection are met.

The continuous copper films became unstable when heated above ≈225 °C. Thermodynamic considerations indicate that Cu does not wet SnO$_2$(010) or (10$\bar{1}$) at equilibrium.[26] Instead, the growth of thick but tiny islands of Cu is expected on most oxide surfaces because Cu–Cu interactions are significantly stronger than Cu–substrate interactions. However, when deposition occurs at sufficiently low temperatures (frequently, at or below room temperature), kinetic constraints can produce laminar films due to diffusion limitations, as is known from studies on several model metal/oxide systems using late transition metals, including palladium on TiO$_2$(110)[27] and MgO(100),[28] platinum on ZnO(0001),[29] and copper on ZnO(0001)-O[30] and SnO$_2$-(110).[31] Campbell et al. have argued that under such conditions of kinetic control, Cu adatoms nucleating the initial 2D metal islands on the oxide surface lack the thermal energy needed to step up onto the widening Cu terraces to

form 3D islands, yet they step down easily, resulting in pseudo-layer-by-layer growth.[32] Continuous and flat metal films are thus expected when the density of nucleation sites is high and/or the amount of deposited metal is large (>10 monolayers), as is the case here.[33] These films are metastable and mild annealing triggers their disintegration into 3D islands separated by clean patches of oxide.

Both the untextured and epitaxial Cu films irreversibly converted to thick, flat islands in the second stage of in situ heating, from 225–500 °C. The sequences of images in Figures 4 and 5 show only subtle differences in the structural evolution of the two film types. Grain growth and surface
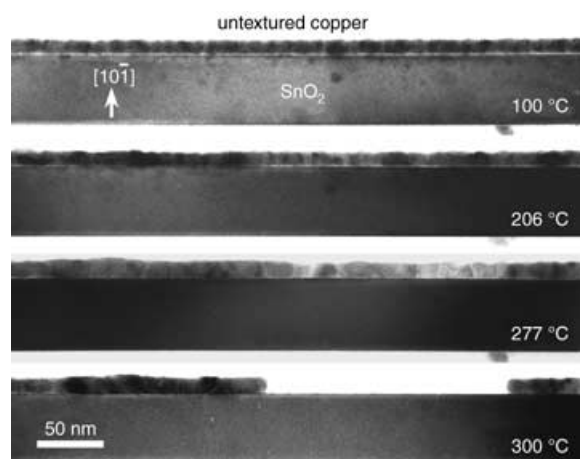

Figure 4. Island formation from an untextured bilayer. A series of TEM images shows that the continuous copper film, with an initial thickness of 11 nm, coarsened and broke up into thick (15–25 nm) and flat islands at 300 °C. The islands remain in the solid phase throughout this process.
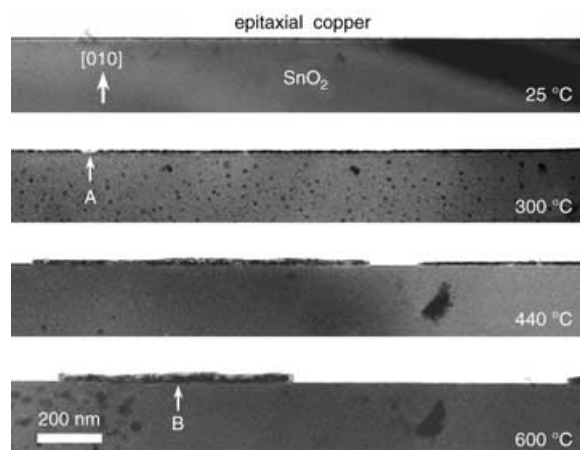

Figure 5. Island formation from an epi-bilayer. Epitaxial copper layers underwent a process of coarsening and island formation similar to that of untextured bilayers, but at a temperature nearly 75 °C higher. The label A denotes a notch forming in the 10-nm-thick Cu film. The island indicated by B is 25−35 nm thick and retains its epitaxial orientation with the ribbon. Dark patches on the basal surface of the ribbon are untextured Cu islands that continuously moved and grew in size during the heating process. Note that the first two and the last two images were acquired from different regions of the same bilayer.

coarsening were evident in both films by $\approx 160\,°C$. On average, untextured Cu films dewet the substrate at $\approx 250\,°C$, approximately $75\,°C$ cooler than epi-layers of the same thickness, presumably because of weaker bonding to the ribbon substrate. The onset of island formation was followed in both cases by a rapid but brief increase in island number and then a sustained period of slow island thickening. At temperatures $200\,°C$ above the onset temperature the islands had grown two to five times thicker than the original films, with island diameters averaging in the hundreds of nanometers. At these intermediate temperatures, copper adatoms were increasingly able to diffuse onto the tops of the islands. This led to the sequential nucleation of new metal layers, resulting in flat Cu mesas, roughly rectangular in shape. The size and shape of these islands is constrained by the very thin SnO_2 surfaces on which they form ($<100\,nm$ wide if electron transparent). Copper films coated onto much wider ribbons broke up into irregular or gumdrop-shaped islands with a wide size distribution (Figure 6). In all cases, they remained pure, solid copper

until about $500\,°C$, when ex situ EDS detected the interdiffusion of a small amount of tin from the substrate. We also found that the untextured islands completely transformed to the thermodynamically preferred Cu(111) orientation when the temperature approached $450\,°C$.

For comparison, we fabricated bilayers at a substrate temperature of $400\,°C$, substantially above the critical temperature for island formation. The resulting copper islands were smaller, more numerous, and more densely packed than the islands formed by post-deposition annealing (Figure 7). We interpret this morphological difference as stemming from two effects: 1) The nanoribbon surfaces are mostly free of adsorbed gases at $400\,°C$, which lowers the density of defects that act as sites for island nucleation and may also decrease the free energy of wetting for Cu on the cleaner oxide, resulting in smaller islands;[34] 2) surface diffusion is not kinetically constrained at $400\,°C$, such that the initial Cu monolayers never coalesce into a continuous film but instead begin to build a large number of thick islands. These findings show that island coalescence and film disintegration are not reversible in time. Once a continuous film has formed, its breakup follows a radically different potential energy surface such that the initial nucleates are generally not recovered.

Above $500\,°C$, the Cu islands underwent a series of solid-state reactions with the underlying SnO_2, leading to several new phases and dramatic changes in morphology. Tin was first incorporated into many of the thickened islands at a concentration of up to a few atomic percent. Concurrent with the accumulation of tin was the formation of sheaths of amorphous Cu–O at the retreating edges of many of the Cu–Sn islands (see Supporting Information, Figure S3). On the SnO_2-($10\bar{1}$) surface, these alloy islands began to etch rapidly into the ribbon substrate at $575\,°C$ (Figure 8), while the (010) surface proved more chemically resistant, with etching starting above $650\,°C$ (see Supporting Information, Figure S4). Because copper is thermodynamically incapable of reducing SnO_2 directly to produce tin suboxides and copper oxides,[35] etching must proceed with the formation of Cu–Sn solid solutions or intermetallic compounds, together with a significant loss of oxygen to vacuum. The fact that EDS detected oxygen only in the nanoribbons and Cu–O sheaths, but never in the Cu–Sn islands themselves, is consistent with
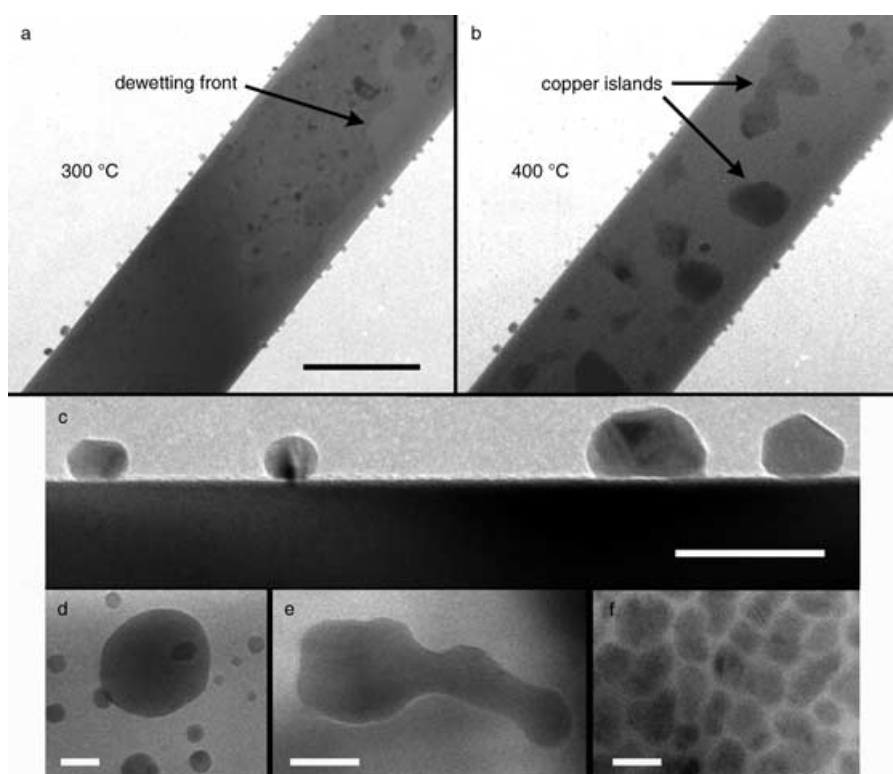

Figure 6. Island formation on wide ribbon substrates, where island shape is unconstrained by substrate size: a,b) Plan-view TEM images of a 550-nm-wide ribbon during the breakup of a 10-nm-thick untextured Cu layer on the ($10\bar{1}$) basal surface. The smooth copper layer retreated from the edges of the ribbon first, maintaining its continuity and leaving behind a small number of Cu particles on the sides of the substrate. Islands with irregular shapes and a large size distribution were formed at $400\,°C$. Scale bar $= 500\,nm$; c) cross-sectional views of Cu particles on both the basal and side surfaces revealed that islands appearing shapeless in projection were often highly faceted in three dimensions. These four islands show various degrees of {100}, {110}, and {111} faceting. Scale bar $= 50\,nm$; d) magnified plan view of Cu islands on the basal surface, showing their large size distribution. Scale bar $= 25\,nm$; e) the assimilation of two small islands by one large island. Scale bar $= 50\,nm$; f) a different breakup morphology. Here, the copper film did not dewet along a single front nucleated from a small number of defects, as in (b). Instead, it disintegrated into a large number of medium-sized islands. Scale bar $= 50\,nm$.
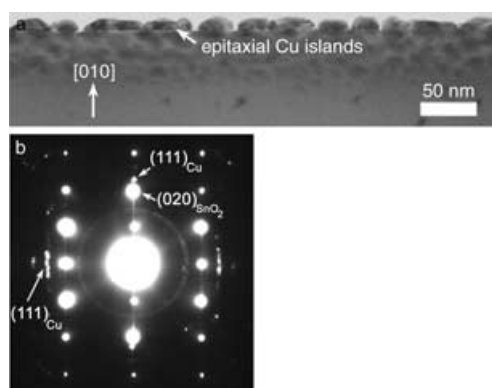
Figure 7. Characterization of an epi-bilayer fabricated at 400 °C: a) The copper film was deposited at a nominal thickness of 10 nm. Small, epitaxial, and mostly flat islands cover over 80 % of the substrate surface; b) SAED of the epi-islands. Some of the islands have orientations that are rotated ≈90° in the plane of the paper.

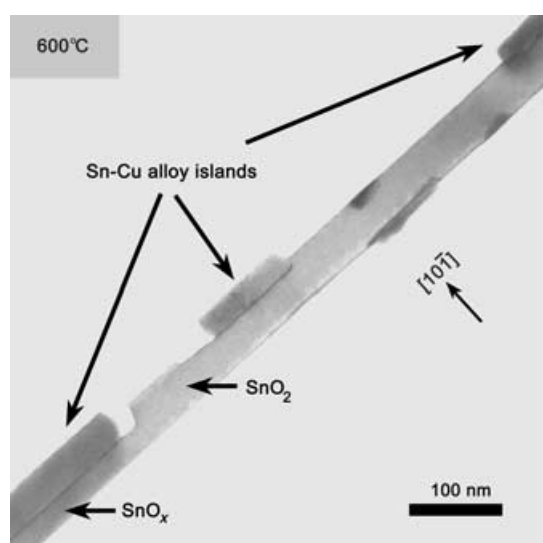**Figure 8.** Etching of the $SnO_2(10\bar{1})$ surface by copper. At 600 °C many of the islands had eroded flat etch pits into the ribbon substrate. Regions underneath the islands were depleted of oxygen, while tin was distributed inhomogeneously in the copper, with higher concentrations near the island–substrate boundaries.

this thermodynamic picture. Diffusion of Cu into the SnO_{2-x} lattice was sometimes observed in regions near island–substrate interfaces. However, tin is known to diffuse readily into solid Cu even at much lower temperatures,[36] and once freed from its oxide, can act as the major diffusing species here as well.

As etching continued, many of the flat islands lost their faceting, assumed quasi-spherical shapes, and burrowed into the underlying SnO_{2-x} (Figure 9). At ≈700 °C a large fraction of these particles had transformed into spheroids of crystalline $Cu_{10}Sn_3$ or other intermetallic phases. The smaller spheroids typically stopped eating through the oxide well before they etched across the entire thickness of the ribbon. Larger islands, however, contained enough metal to completely sever a ribbon, with the result that most ribbons
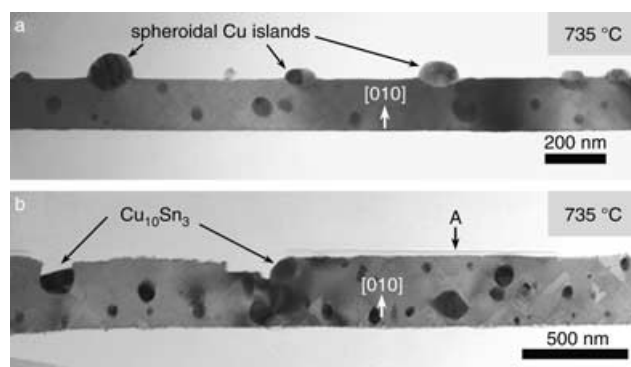

Figure 9. Etching of the (010) surface at high temperature. The original copper film was 8 nm thick. a) The alloy islands assumed spherical shapes starting at around 675 °C and many transformed into crystalline intermetallic phases, some of which were positively identify by SAED; b) in another region of the same ribbon, small spheroids of $Cu_{10}Sn_3$ had etched deep into the substrate at 735 °C. The label A denotes the residual Cu–O sheath left behind by the departed Cu–Sn islands.

were diced into multiple segments of jagged SnO_{2-x} capped on both ends by agglomerates of Cu–Sn covered with shells of suboxides (Figure 10). The ribbons were destroyed in this way just as several of the Cu–Sn phases began to liquefy at ≈775 °C, which was also the highest temperature reached in our experiments.

3. Conclusions

Each stage in the sequence of bimetallic bending, island formation, and etching involves a number of fundamental processes that have only received brief mention here and could form the basis of future, more detailed studies. We have shown that the bilayer nanoribbon is a useful platform for such studies using in situ TEM. The large number of available ribbons and interesting ribbon/coating combinations make this a promising approach for investigating adhesion, faceting, interdiffusion, and other interfacial effects between different classes of materials. Bilayer nanoribbons are also extremely sensitive thermal probes that could be used in future nanocantilever-based calorimetry and biosensing schemes.

4. Experimental Section

SnO_2 nanoribbons were synthesized by a vapor transport process described in detail elsewhere.[5,11] Ribbons were brushed onto mesh-free, thin bar nickel TEM grids and coated with copper (99.999 %) in a home-built thermal evaporator (with a base pressure of 2×10^{-7} Torr) using a glancing geometry (with the grid nearly parallel to the metal flux) and a deposition rate of 0.3 Å s^{-1} at a pressure of $4–8 \times 10^{-7}$ Torr. The glancing geometry yielded bilayers that were pinned to the grid at one end and properly oriented for viewing along the metal/oxide interface.
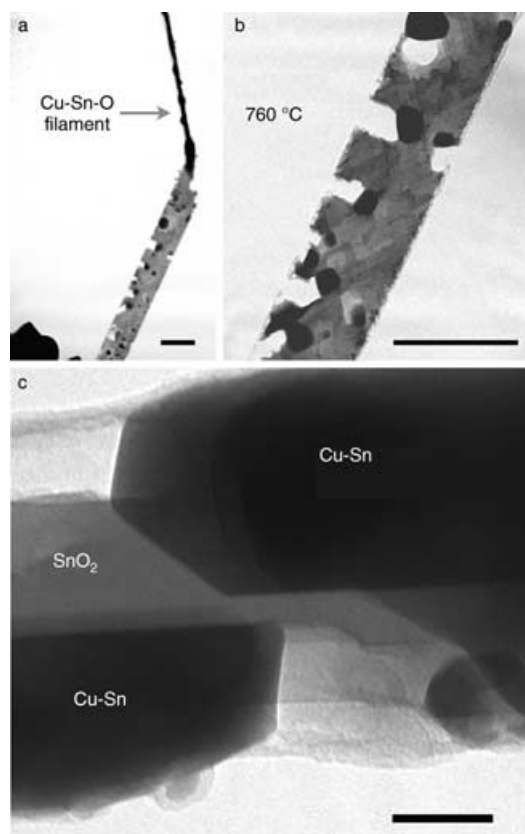
Figure 10. Massive etching and destruction of SnO_2 nanoribbons by metal islands: a) A severed ribbon at 760 °C. Here, a large Cu–Sn island ate through the oxide substrate and was pulled into a long filament by the weight of the suspended length of the ribbon. Eventually the suspended section fell away, leaving behind a free Cu–Sn–O filament. This process occurred wherever large islands had segregated. The original bilayer consisted of 100 nm of Cu on 410 nm of SnO_2. Scale bar = 500 nm; b) magnified view of the Cu–Sn spheroids burrowing into the oxide substrate. Note the point where the ribbon is soon to be severed by two advancing metal droplets. Scale bar = 500 nm; c) a break point on a different ribbon (9 nm epi-Cu on a 90 nm ribbon), just before the metal islands coalesced. This sample suffered abnormally large amounts of carbon deposition from the electron beam. Scale bar = 25 nm.

Structural and chemical characterizations were performed in a 200 kV Philips CM200 microscope, while a JEOL 3010 (300 kV) equipped with a double-tilt heating stage was used for in situ experiments. Heating and cooling rates were ≈5 °C min^{-1}. Bending data were extracted from images acquired in 25 °C increments from 25–200 °C, with each sample undergoing at least three heating/cooling cycles for comparison. Direct heating effects from the electron beam were negligible at the low magnifications used in this study; bilayers held under the beam for hours at room temperature showed no bending or changes in microstructure. Surface carbon contamination was frequently seen above ≈300 °C as a thin (<1 nm) discontinuous layer of amorphous material. Because heavy carbon contamination was found to alter the dynamics of island formation, we have discussed here only the data for the cleanest samples.

[1] C. Heske, *Appl. Phys. A* **2004**, *78*, 829–835.
[2] C. Bressler, M. Chergui, *Chem. Rev.* **2004**, *104*, 1781–1812.
[3] W. J. Kaiser, L. D. Bell, *Phys. Rev. Lett.* **1988**, *60*, 1406–1409.
[4] V. Maurice, G. Despert, S. Zanna, M.-P. Bacos, P. Marcus, *Nat. Mater.* **2004**, *3*, 687–691.
[5] Z. W. Pan, Z. R. Dai, Z. L. Wang, *Science* **2001**, *291*, 1947–1949.
[6] T. Kizuka, N. Tanaka, *Phys. Rev. B* **1997**, *56*, R10079–R10082.
[7] H. Tanaka, T. J. Konno, R. Sinclair, N. Hirashita, *J. Appl. Phys.* **1995**, *78*, 4982–4987.
[8] P. L. Hansen, J. B. Wagner, S. Helveg, J. R. Rostrup-Nielsen, B. S. Clausen, H. Topsøe, *Science* **2002**, *295*, 2053–2055.
[9] Z. L. Wang, Z. R. Dai, R. P. Gao, Z. G. Bai, J. L. Gole, *Appl. Phys. Lett.* **2000**, *77*, 3349–3351.
[10] J. Hu, Y. Bando, Z. Liu, T. Sekiguchi, D. Golberg, J. Zhan, *J. Am. Chem. Soc.* **2003**, *125*, 11306–11313.
[11] R. He, M. Law, R. Fan, F. Kim, P. Yang, *Nano Lett.* **2002**, *2*, 1109–1112.
[12] J. Narayan, B. C. Larson, *J. Appl. Phys.* **2003**, *93*, 278–285.
[13] T. Wagner, J. Marien, G. Duscher, *Thin Solid Films* **2001**, *398–399*, 419–426.
[14] G. V. Samsonov, *The Oxide Handbook*, Plenum, New York, **1973**.
[15] R. J. Roark, W. C. Young, *Roark's Formulas for Stress and Strain*, 6th ed., McGraw-Hill, New York, **1989**.
[16] E. Chang, E. K. Graham, *J. Geophys. Res.* **1975**, *80*, 2595–2599.
[17] H. Hellwig, A. F. Goncharov, E. Gregoryanz, H. Mao, R. J. Hemley, *Phys. Rev. B* **2003**, *67*, 174110.
[18] Y. Zheng, R. E. Geer, *Mater. Res. Soc. Symp. Proc.* **2004**, *821*, P2.3.1–P2.3.6.
[19] J. Schiøtz, K. W. Jacobsen, *Science* **2003**, *301*, 1357–1359.
[20] J. R. Barnes, R. J. Stephenson, C. N. Woodburn, S. J. O'Shea, M. E. Welland, T. Rayment, J. K. Gimzewski, C. Gerber, *Rev. Sci. Instrum.* **1994**, *65*, 3793–3798.
[21] R. Berger, E. Delamarche, H. P. Lang, C. Gerber, J. K. Gimzewski, E. Mayer, H.-J. Güntherodt, *Science* **1997**, *276*, 2021–2024.
[22] G. Wu, H Ji, K. Hansen, T. Thundat, R. Datar, R. Cote, M. F. Hagan, A. K. Chakraborty, A. Majumdar, *Proc. Natl. Acad. Sci. USA* **2001**, *98*, 1560–1564.
[23] X. Wang, Y. Ding, C. J. Summers, Z. L. Wang, *J. Phys. Chem. B* **2004**, *108*, 8773–8777.
[24] E. Meyer, J. K. Gimzewski, C. Gerber, R. R. Schlittler in *The Ultimate Limits of Fabrication and Measurement* (Eds.: M. E. Welland, J. K. Gimzewski), Kluwer, Dordrecht, **1995**, pp. 89–95.
[25] S. A. Chambers, T. Droubay, D. R. Jennison, T. R. Mattsson, *Science* **2002**, *297*, 827–831.
[26] The thermodynamic condition for the perfect wetting of a metal on an oxide surface is $\gamma_{interface} = \gamma_{oxide} - \gamma_{metal}$, where the terms refer to the free energies of the metal/oxide interface and the clean oxide and metal surfaces, respectively. If $\gamma_{interface} > \gamma_{oxide} - \gamma_{metal}$ then the metal does not wet the oxide surface. Calculations (Refs. [39] and [40]) show that the free energy of SnO_2{101} and {010} is markedly lower than that of Cu{111} (1.2–1.35 J m^{-2} versus 1.8–1.95 J m^{-2}). In general, Cu–oxide

bonding typically involves mostly weak polarization interactions (minimal charge transfer), meaning that $\gamma_{interface}$ is large and 3D islands should exist at equilibrium.

[27] J. Evans, B. E. Hayden, G. Lu, *Surf. Sci.* **1996**, *360*, 61–73.

[28] C. R. Henry, C. Chapon, C. Duriez, S. Giorgio, *Surf. Sci.* **1991**, *253*, 177–189.

[29] W. T. Petrie, J. M. Vohs, *J. Chem. Phys.* **1994**, *101*, 8098–8107.

[30] K. H. Ernst, A. Ludviksson, R. Zhang, J. Yoshihara, C. T. Campbell, *Phys. Rev. B* **1993**, *47*, 13782–13796.

[31] Z. Li, Q. Guo, P. J. Møller, *Z. Phys. D* **1997**, *40*, 550–553.

[32] C. T. Campbell, *Surf. Sci. Rep.* **1997**, *27*, 1–111.

[33] Model oxide surfaces typically have a low density of defects to act as nucleation sites, so that for certain systems 2D metal islands stop growing laterally and start growing vertically before they coalesce into a continuous layer. This results in 3D islands that cover a substantial fraction of the substrate. In contrast, the nanoribbons are rich enough in surface defects (e.g., step edges and adsorbates) to nucleate a high density of islands that coalesce before reaching their critical size (see Refs. [32] and [37]).

[34] A. Sandell, J. Libuda, M. Bäumer, H.-J. Freund, *Surf. Sci.* **1996**, *346*, 108–126.

[35] SnO_2 is at least 250 kJ mol^{-1} more stable than either Cu_2O or CuO at the temperatures and oxygen partial pressure relevant here (see Ref. [38]).

[36] Y. Wu, E. G. Jacobs, C. Pouraghabagher, R. F. Pinizzotto, *Mater. Res. Soc. Symp. Proc.* **1994**, *323*, 165–170.

[37] L. V. Koplitz, O. Dulub, U. Diebold, *J. Phys. Chem. B* **2003**, *107*, 10583–10590.

[38] L. S. Darken, R. W. Gurry, *Physical Chemistry of Metals*, McGraw-Hill, New York, **1953**.

[39] A. Beltrán, J. Andrés, E. Longo, E. R. Leite, *Appl. Phys. Lett.* **2003**, *83*, 635–637.

[40] L. Vitos, A. V. Ruban, H. L. Skriver, J. Kollár, *Surf. Sci.* **1998**, *411*, 186–202.